Hybrid PET-MRI Imaging for Radiotherapy Treatment Response Assessment: Prognostic Value and Current Challenges

Deanna Pafundi, Ph.D., DABR
Assistant Professor, Mayo Clinic

2020 Virtual AAPM

No Disclosures

Learning Objectives

- 1) Understand the basic principles behind PET-MRI technology
- 2) Identify applications of quantitative imaging to assess treatment response in RT using PET-MRI technology
- 3) Understand the challenges related to application in quantitative imaging for treatment response assessment using PET-MRI technology

MAYO CLINIC

Why complicate things?

- We have PET-CT to give us anatomical and functional information. Isn’t that enough?

MAYO CLINIC

PET-MRI Versus PET-CT

TABLE I: Advantages of PET/MRI Versus PET/CT

Attribute	PET/MRI Advantages	PET/CT Advantages
Lesion detection	Improved lesion detection in the brain, breast, liver, kidneys, and bone	No advantage
Lesion margins	Better delineation of T category in nonpulmonary soft tissues and bone	Improved delineation of lesion margins within lung parenchyma
Lesion alignment	Better alignment of simultaneously acquired PET/MRI data compared with PET/CT	No advantage
Quantitative accuracy	Improved quantification by MRI-based motion correction without additional radiation	Industry standard (i.e., attenuation) is based on density seen on CT
Scanning time	No advantage	PET/CT body scanning protocols currently faster
Radiation exposure	Lack of CT reduces radiation exposure (up to 50% depending on CT protocol)	No advantage
Patient convenience	Single appointment for patients who require both PET and MRI; less scanner time overall	No advantage
Multiparametric quantitative imaging	Expanded capabilities such as DWI, perfusion MRI, and spectroscopy	No advantage
Availability	No advantage	More clinically available

Rosenkrantz *et al*. Current status of Hybrid PET/MRI in Oncologic Imaging. AJR 206, Jan 2016

MAYO CLINIC

Why complicate things?

- We have PET (PET/CT) scanners, we have MRI scanners, can't we just register the two scans and call it a day?
  - Time
  - Acquisition technique and anatomical differences
  - Registration uncertainties (rigid/deformable)

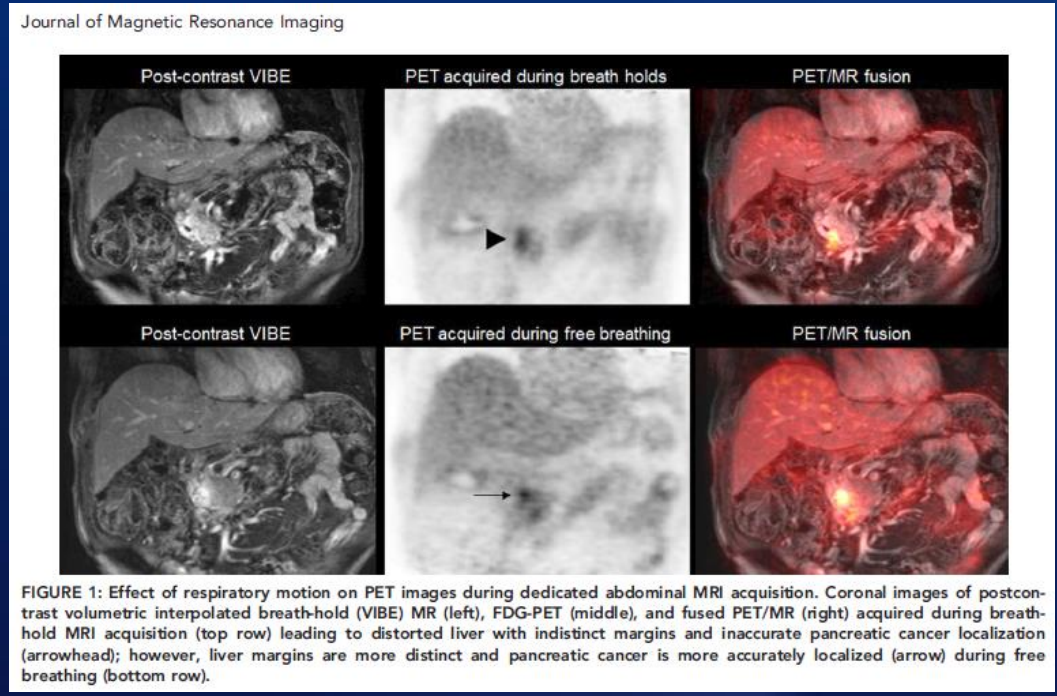

FIGURE 1: Effect of respiratory motion on PET images during dedicated abdominal MRI acquisition. Coronal images of postcontrast volumetric interpolated breath-hold (VIBE) MR (left), FDG-PET (middle), and fused PET/MR (right) acquired during breath-hold MRI acquisition (top row) leading to distorted liver with indistinct margins and inaccurate pancreatic cancer localization (arrowhead); however, liver margins are more distinct and pancreatic cancer is more accurately localized (arrow) during free breathing (bottom row).

Sotoudeh H. *et al*. Clinical Application of PET/MRI in Oncology. J. MAGN. RESON. IMAGING 44:265-276, 2016

PET-MRI Challenges: Design Considerations

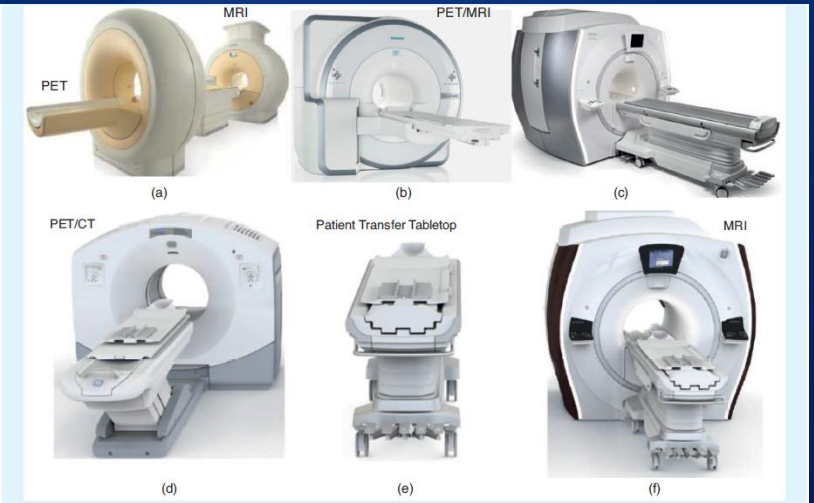

FIGURE 2. (a)–(c) The Philips Healthcare whole-body Ingenuity TF PET/MRI system [in which a turntable patient-handling system facilitates patient motion between the PET subsystem shown in (a) and the Achieva 3T X-series MRI system shown in (c) for sequential acquisition], the Siemens Healthcare Biograph mMR system, and the GE Healthcare SIGNA PET/MRI system, enabling simultaneous acquisition of PET and MRI data. (d)–(f) The GE Healthcare trimodality (PET/CT and MRI) setup using a dedicated patient transporter tabletop. [(a) and (c) used courtesy of Philips Healthcare, (b) courtesy of Siemens Healthcare, and (d)–(f) courtesy of GE Healthcare.]

Table 1. The main features of currently available clinical PET/MRI systems.

System	Manufacturer	Operation	PET detector/readout	Axial FOV (cm)	TOF	MRI	Reference
Biograph mMR	Siemens Healthcare	Simultaneous	LSO/APDs	25.8	No	Verio 3T (modified)	[29]
Ingenuity TF	Philips Healthcare	Sequential	LYSO/PMTs	18	Yes	Achieva 3T	[24]
Signa PET/MRI	GE Healthcare	Simultaneous	LYSO/SiPMs	25	Yes	MR750w 3.0T (modified)	[17]
Trimodality	GE Healthcare	Sequential	LYSO/PMTs	15.7	Yes	MR750w 3.0T	[25]
BrainPET	Siemens Healthcare	Simultaneous	LSO/APDs	19.2	No	Trio 3T (modified)	[30]
Brain MGI	Academia	Sequential	LSO-LYSO/PMTs	25.2	No	Magnetom 7T	[26]

Adapted with permission from [23].

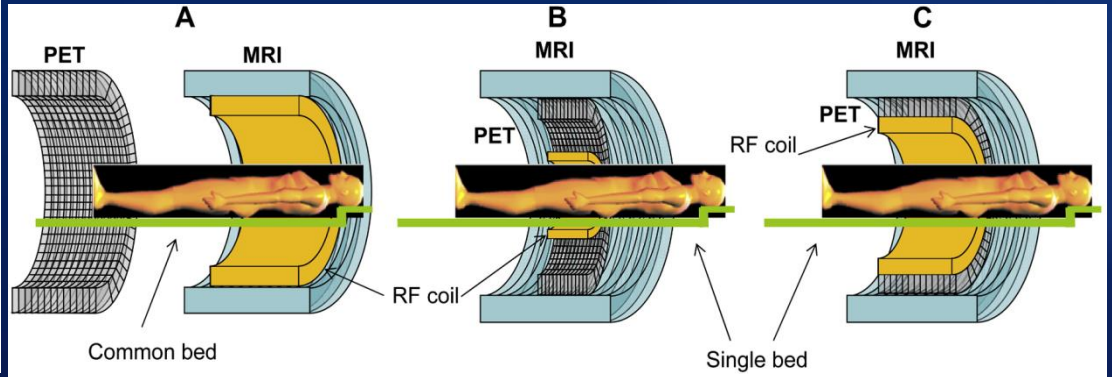

Fig 1 Schematic cross-sectional views of potential designs for combined PET/MR imaging systems: (A) tandem design with two imagers mounted back-to-back (similar to that in PET/CT instrumentation) to allow sequential rather than simultaneous acquisition, (B) insert design with PET imager inserted between radiofrequency coil and gradient set of MR imager, and (C) fully integrated design with two imagers in same gantry. Radiofrequency (RF) coil, gradient set, PET imager, and patient bed are shown for all configurations.

Torigian *et al*. PET/MR Imaging: Technical Aspects and Potential Clinical Applications. *Radiology* 267 (1): 2013.
Zaidi, Habib. A Pivotal Time for Hybrid PET/MR Imaging Technology. *JACR* 10 (11), P878-881. 2013.
Zaidi H. and Becker M. The Promise of Hybrid PET/MRI: Technical advances and clinical applications. *IEEE Signal Processing Magazine* pp. 67-85: May 2016.

PET-MRI Challenges: Design Considerations

- Positron range reduction
- Avalanche diodes and Si PMTs

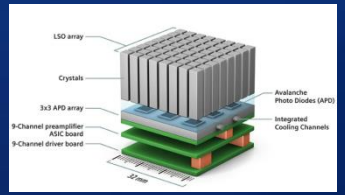

- TOF Resolution

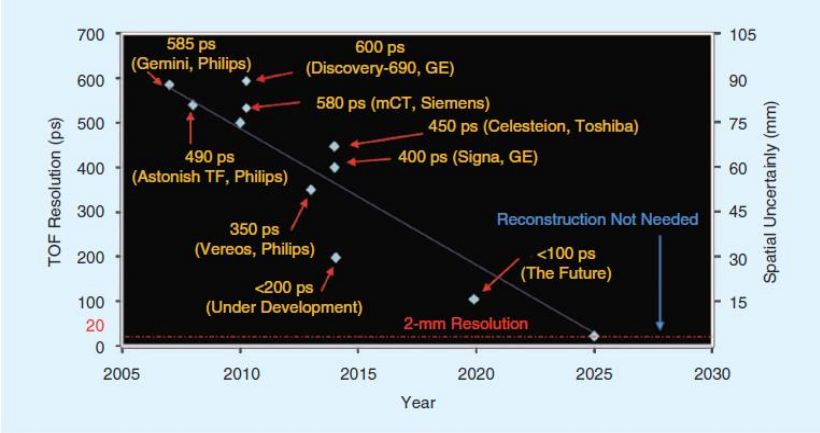

FIGURE 3. The evolution of TOF resolution performance characteristics of current-generation and future-generation TOF PET scanners. PS: picoseconds.

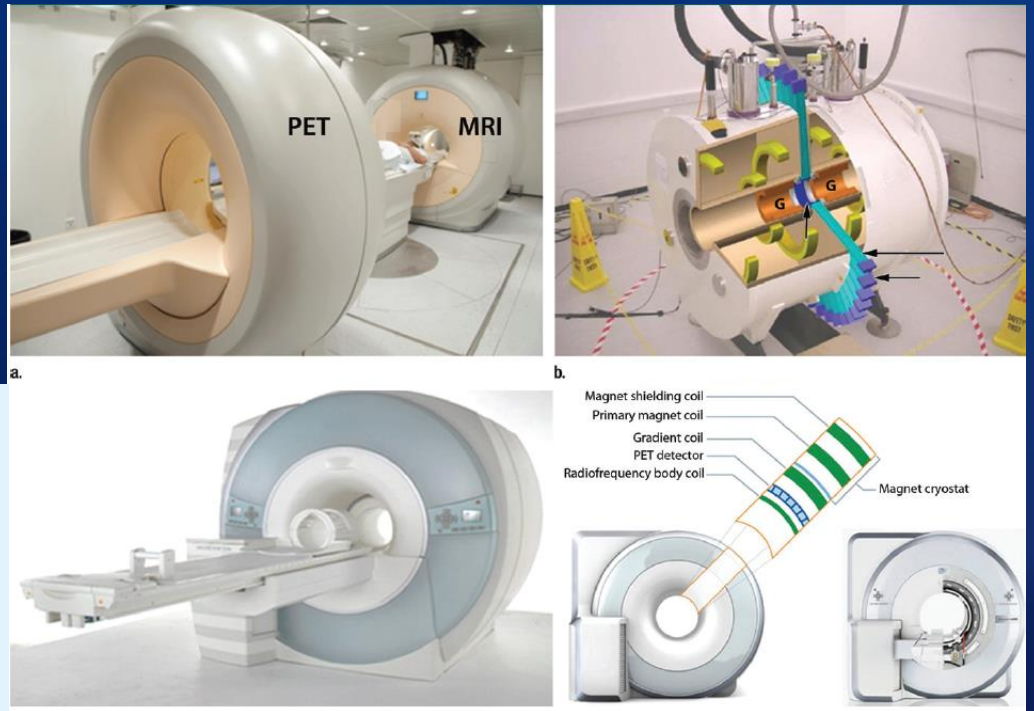

Figure 2: Representative PET/MR imaging instruments. **(a)** Photograph of whole-body Ingenuity TF PET/MR imaging system (Philips Healthcare) installed at Geneva University Hospital, Switzerland. Turntable system facilitates patient motion between Achieva X series 3-T MR imaging system on right and time-of-flight PET system on left. **(b)** Cutaway schematic of split-magnet of PET/MR imaging shows scintillation crystal ring (vertical arrow), fiber bundles (horizontal long arrow), screened photomultiplier tubes outside magnet cryostat (horizontal short arrow), and split gradient coil *(G)*. (Modified and reprinted, with permission, from reference 28.) **(c)** Photograph of integrated BrainPET PET/MR imaging design (Siemens Healthcare) consists of isocentric layering of MR imaging head coil, PET detector ring, and MR imaging magnet tunnel. **(d)** Schematic view of whole-body Biograph mMR PET/MR imaging prototype showing basic system components in which PET detector ring is placed between radiofrequency coil and gradient coil. (Image courtesy of Siemens Healthcare.)

Torigian *et al*. PET/MR Imaging: Technical Aspects and Potential Clinical Applications. *Radiology* 267 (1): 2013.
Zaidi H. and Becker M. The Promise of Hybrid PET/MRI: Technical advances and clinical applications. *IEEE Signal Processing Magazine* pp. 67-85: May 2016.

PET-MRI Challenges: Attenuation Corrections

- MRI signal NOT correlated with electron density like CT

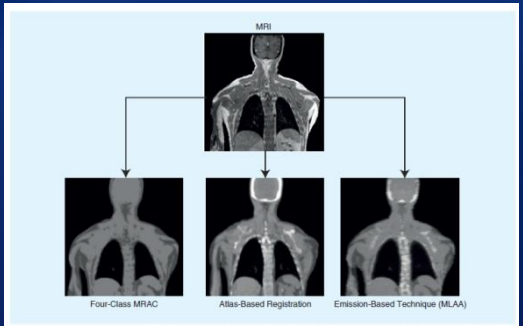

FIGURE 5. Strategies for MRI-guided attenuation map generation, including the four-class segmentation-based method, atlas-based registration and machine learning, and MRI-guided emission-based technique (MLAA). MRAC: MRI-based attenuation correction. (Figure adapted with permission from [37].)

TABLE III. Comparison of pros and cons of the different categories of MRAC techniques used in PET/MRI.

	Segmentation-based	Atlas-based	Emission-based
Computation speed	+++	+	—
Simplicity and robustness	+++	+	+
Patient-specificity of lung LACs	—	+	++
Patient-specificity of bone LACs	—	++	++
Specific data requirement	—	+	+
MR truncation compensation	—	—	++
Coil attenuation estimation	—	—	+
MR susceptibility artifact reduction	—	+	++
Respiratory artifact reduction	—	—	+

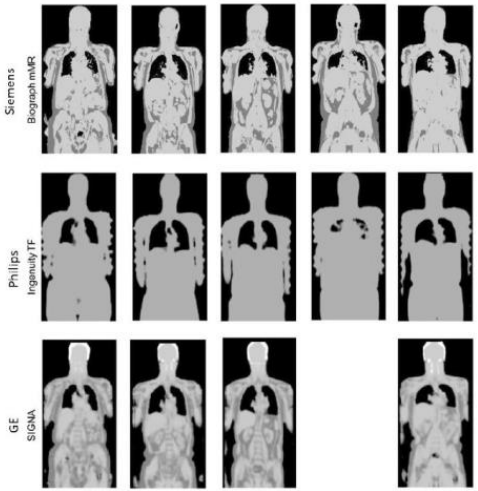

FIG. 8. Example magnetic resonance attenuation correction (MRAC) maps from the three major vendors. Adapted from Beyer et al.[66] Note that the Siemens MRAC images were obtained using the older software version "VB18P", and at this time, bone was not included as a separate tissue class.

- 3 Main Categories of Attenuation Techniques:
  - Segmentation-based MRAC (limited to brain)
  - Atlas-Based Registration
  - Emission-Based Technique (MLAA)

Zaidi H. and Becker M. The Promise of Hybrid PET/MRI: Technical advances and clinical applications. *IEEE Signal Processing Magazine* pp. 67-85: May 2016.
A. Mehranian, H. Arabi, and H. Zaidi, "Magnetic resonance imaging-guided attenuation correction in PET/MRI: Challenges, solutions and opportunities," *Med. Phys.*, vol. 43, no. 3, pp. 1130–1155, Mar. 2016.
Lillington J. et al. PET/MRI attenuation estimation in the lung: A review of past, present, and potential techniques. Med Phys. 47(2), February 2020.

PET-MRI Challenges: Attenuation Corrections

TABLE I. Overview of MRI-guided attenuation correction strategies in PET/MRI.

Category	Body region	Technique and data	Tissue classes (attenuation values)	Key advantages of the method/findings of study	Limitations	Quantification errors
Segmentation-based methods (Sec. 2.A)		Segmentation of T1W MRI using supervised fuzzy C-means clustering (Ref. 21)	Brain tissue (0.099 cm^{-1}), skull (0.14 cm^{-1}), nasal sinuses (0.054 cm^{-1}), and air (0 cm^{-1})	Inclusion of bones	Semiautomatic segmentation of bones	2.4% bias using ten patients in comparison to transmission μ-maps
		Neural network-based segmentation of MP-RAGE MRI (Refs. 22 and 24)	Air (0 cm^{-1}), brain tissue (0.096 cm^{-1}), skull (0.146 cm^{-1}), and Mastoid process (0.054 cm^{-1})	Fully automatic, knowledge-based	Mis- or oversegmentation of bones in the presence of abnormal anatomy or pathology	−6.1% to 2.7% bias in cortical regions and −7.0% to 5.6% for subcortical regions using four patients
		Segmentation of dual-echo UTE MRI using region-growing and thresholding (Ref. 12)	Air (0 cm^{-1}), soft tissue (0.096 cm^{-1}), and bones (0.12 cm^{-1})	Direct segmentation of bones	Long acquisition time (6 min), mis-segmentation at air–tissue interfaces	Average 5% error in brain tissues of five PET/CT/MRI patients
	Brain	Segmentation of dual-echo UTE MRI using morphological closing and arithmetical operations (Ref. 11)	Air (0 cm^{-1}), soft tissue (0.096 cm^{-1}), and bones (0.136 to 0.180 cm^{-1})	Direct segmentation of bones, 3.3 min acquisition time	Poor spatial resolution of UTE data, mis-segmentation at air–tissue interfaces	Bone LACs of 0.143 and 0.151 cm^{-1} resulted in best bias variability trade-off in quantification
		Segmentation of triple-echo UTE MRI using thresholding and morphological filtering (Ref. 25)	Air (0 cm^{-1}), soft tissue (0.1 cm^{-1}), fat (0.09 cm^{-1}), and bones (0.172 cm^{-1})	Direct segmentation of bones and inclusion of fat	Bone misclassifications at paranasal sinuses	Over 80% of bone voxels were correctly classified in six studied patients
		Segmentation of Dixon fat and water MRI (Ref. 19)	Air, soft-tissue fat	Radial variation of quantification errors when bones are ignored	Presence of metal-induced artifacts in MRAC maps	SUV bias of 25% in cortical regions and 5%–10% in central regions of the brain (19 patients)
		Segmentation of 3D T1 SPGR MRI using deformable shape modeling and thresholding (Ref. 16)	Air, lungs, and soft tissue	Fast, fully automatic	Bone/air and lung segmentation challenging, truncation artifacts, etc.	<10% SUV bias in malignant soft-tissue lesions with respect to CTAC, −12% bias in a pelvis lesion (15 patients)
	Whole-body	Segmentation of two-point Dixon MRI (Ref. 26)	Air, lungs, and soft and fat tissues	Inclusion of fat tissue, fast	Same as above	−8% SUV bias in bone lesions (35 patients)
		Phase-field-based segmentation and mapping of two-point Dixon MRI (Ref. 27)	Continuous fat/water (0.086–0.1 cm^{-1}), lungs, and air	Continuous fat and water LACs	Same as above	Mean SUV bias of 10% in the liver and −2% in malignant lesions (16 patients)
Atlas-based segmentation, registration and machine learning methods (Sec. 2.B)	Brain (without UTE)	Patch-based Gaussian process regression and atlas registration (Ref. 28)	Continuous	Robust to misregistration errors	Very time-consuming (Gaussian process regression)	Mean SUV bias of 3% for predefined regions of interest with respect to CTAC
		Voxelwise classification of air/bone from MRI without atlas registration using random forest method (Ref. 29)	Binary	No need for atlas registration, time efficient	Susceptible to presence of artifacts in MR image	Dice values of 0.83 ± 0.08 and 0.98 ± 0.01 for air and bone, respectively
		Voxelwise atlas fusion using LNCC as image similarity measure (Ref. 30)	Continuous	Very robust to misregistration errors	Time-consuming (40 atlas registrations are required)	Relative absolute error of 5% for the full head with respect to CTAC
		Patch-based pseudo-CT generation without using deformable atlas registrations (Ref. 31)	Continuous	No need for atlas registration, time efficient	—	Dice values of 0.84 ± 0.02 for bone volume
	Brain (with UTE)	Pseudo-CT generation by including spatial information into Gaussian mixture regression (Ref. 32)	Continuous	Robust pseudo-CT generation using UTE sequence	Requires four UTE images with different echo times and flip angles	Mean absolute prediction deviation of 130 ± 18 HU with spatial information
		Patient-specific bone attenuation coefficient estimation based on UTE (Please check, and correct if necessary.Ref. 33)	Continuous bone, air (0 cm^{-1}), fat (0.092 cm^{-1}), and soft-tissue (0.1 cm^{-1})	Patient-specific bone attenuation coefficient	Requiring UTE and Dixon sequences	Dice values of 0.75 ± 0.05 across 98 subjects for bone and 0.60 ± 0.08 for sinus air cavities
		Patch-based pseudo-CT generation via Bayesian framework (Ref. 34)	Continuous	No atlas registration and segmentation required	—	PET pseudo-CT AC exhibited correlation coefficient of 0.99 with respect to PET-CTAC
	Whole-body	Gaussian process regression and atlas registration (Ref. 35)	Continuous	Robust to misregistration errors	High computational time	In regions of normal physiologic uptake, the average bias was 8% ± 8% and for lesions was 6% ± 5%
		Gaussian process regression and tissue segmentation (Ref. 36)	Continuous bone, lung (0.024 cm^{-1}), fat (0.0856 cm^{-1}), nonfat (0.1007 cm^{-1}), and Fat/soft-tissue mixture (0.0988 cm^{-1})	Robust to metal induced artifact in MR images	—	SUV bias of 24% ± 6% for lesions near bone and 0.6 ± 11.1% for lesions affected by MR susceptibility artifacts
		Most similar single atlas registration (Ref. 37)	Continuous	Very time efficient (only one atlas registration)	Lack of multiatlas consensus	SUV bias in bony regions ranging from −3% to 4% and −2.1% to 2.6% for lean tissue
		Improved Gaussian process regression with sorted atlas registration (Ref. 38)	Continuous	Very robust to misregistration errors, patient-specific lung LACs	High computational time	Up to 4% lung SUV bias (14 patients)
Emission- and transmission-based methods (Sec. 2.C)		Attenuation estimation using consistency conditions of TOF Radon transform (Ref. 39)	Continuous	Estimation of attenuation sinogram and analytical reconstruction	ACFs are determined up to a constant scaling factor	—
		Maximum likelihood reconstruction of attenuation and activity (MLAA) only TOF EM data (Ref. 40)	Continuous	Patient-specific LACs	Estimated LACs should be corrected for a missing scale factor	—
		MRI-guided MLAA using anatomical regions (Ref. 41)	Discrete LACs (depending on the number of MR regions)	Reduced noise and cross talks in estimated mu maps	Unsolved scale factor, MRI mis-segmentation errors, limited tissue heterogeneity	Bias of −6% in the lungs, −10% in bones, −3% in soft tissues (only one patient)
	Whole-body	MLAA using MR-constrained Gaussian mixture models (Ref. 42)	Continuous, mean LACs of lungs, fat, soft tissue, and bones: 0.027, 0.086, 0.097, 0.104 cm^{-1}	Solved the scale problem, robust to MRI-segmentation errors	Selection of regularization parameters, registration of a bone probability map	Bias of −4% in the lungs, −10% in bones, and −5.0% in soft tissues/lesions (five patients)
		Attenuation estimation from transmission data acquired in simultaneous transmission and TOF PET scanning (Ref. 43)	Continuous, mean LACs of lungs and soft tissue: 0.019 and 0.098 cm^{-1}, respectively	Patient-specific LACs with simultaneous transmission and emission scanning	External transmission source is required, imperfect separation of transmission and emission data results in scaling the LACs, increased radiation dose	−10% in the lungs and soft tissues and −15% in bones (five patients)
		Attenuation estimation from transmission and emission (Ref. 44)	Continuous	Solved the scale problem and improved performance	External transmission source is required, increased radiation dose	—

A. Mehranian, H. Arabi, and H. Zaidi, “Vision 20-20: Magnetic resonance imaging-guided attenuation correction in PET/MRI: Challenges, solutions and opportunities,” *Med. Phys.*, vol. 43, no. 3, pp. 1130–1155, Mar. 2016.

PET-MRI Challenges: Workflow Optimization and Protocol Design

- Literature review of workflow considerations, protocol design and sequence optimization

TABLE 1. Publications Addressing PET/MRI Workflow Considerations, Protocol Design, and Sequence Optimization

Fowler et al. Whole-body simultaneous positron emission tomography (PET)-MR: optimization and adaptation of MRI sequences (11).
Von Schulthess et al. Workflow considerations in PET/MR imaging (12).
Vargas et al. Approaches for the optimization of MR protocols in clinical hybrid PET/MRI studies (13).
Barbosa et al. Workflow in simultaneous PET/MRI (14).
Martinez-Möller et al. Workflow and scan protocol considerations for integrated whole-body PET/MRI in oncology (15).
Kalemis et al. Sequential whole-body PET/MR scanner: concept, clinical use, and optimization after two years in the clinic. The manufacturer's perspective (5).
Reiner et al. Protocol requirements and diagnostic value of PET/MR imaging for liver metastasis detection (16).

Fraum *et al*. PET/MRI: Emerging Clinical Application in Oncology. Academic Radiology 23(2), Feb 2016

- Example of simultaneous Pet/MRI protocol acquisition

TABLE 1. Institutional PET/MR Protocol Overview

1. Fast view localizers
2. Dixon AC sequences (all stations)
3. Transverse T2 HASTE (all stations)
4. PET acquisition (simultaneous with #2 and #3)
5. Specific noncontrast or contrast-enhanced sequences based on study indication[a]

[a]PET data may be acquired simultaneously during any additional MR sequence, and is also tailored to the study indication, eg, early acquisition, delayed, or dynamic acquisition.

TABLE 2. Nominal Values

	MR sequence	TR (msec)	TE (msec)	Slice thickness (mm)	Base resolution	Fat suppression	Orientation
1.	FastView_FoV	2.56	1.44	5	96	None	Transversal
2.	Whole-body PET	3.6	1.23/2.46	3.12	192	None	Coronal
3.	fl3d_vibe_AC	3.6	1.23/2.47	3.12	192	None	Coronal
4.	T2 HASTE	3000	116	5	320	-	Transversal
5.	ep2d_diff (DWI_B50-500-800)	8100	85	5	128	SPAIR	Transversal
6.	T2 SPACE	1710	88	1.5	320	None	Transversal
7.	VIBE_pelvis	3.53	1.25	3	320	Q-fat sat.	Transversal
8.	OPP_IN_TRA	196	1.23/2.46	6	256	None	Transversal
9.	T2_IR_TRA	4140	93	5	256	None	Transversal
10.	Liver VIBE	3.53	1.25	3	320	Q-fat sat.	Transversal
11.	VIBE coronal	4.11	1.83	3	320	Q-fat sat.	Transversal

PET acquisition
2-3 minutes/bed position. Reconstruction: 3D-OSEM. 3 iterations and 21 subsets; 4 mm FWHM Gausian smoothing and Zoom factor of 1

Sotoudeh H. *et al*. Clinical Application of PET/MRI in Oncology. J. MAGN. RESON. IMAGING 44:265-276, 2016

Clinical Applications – Treatment Response Assessment

Clinical Applications – Cervix Cancer

- Baseline, week 2, week 4, post treatment
- FMISO and DCE1min negative correlation

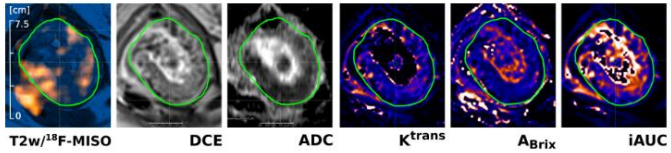

Fig. 1. A representative image dataset (Patient 1 at baseline). [^{18}F]FMISO is windowed to TBR values >1.4 and presented overlaid with the T2w image dataset. The GTV is delineated in green. *Footnote:* Abbreviations: T2w – T2 weighted magnetic resonance imaging, ^{18}F-MISO – tumor to background ratio for [^{18}F]fluoromisonidazole signal, DCE – dynamic contrast enhanced magnetic resonance imaging 1 min after injection, ADC – apparent diffusion coefficient map, K^{trans} – transfer coefficient map of the Tofts model, A_{Brix} – amplitude map of the Brix model, iAUC – map of the initial area under the enhancement curve.

Table 3
Imaging parameters' mean correlations over all patients in all time points and parameters' self-correlations between neighboring time points. DCE_{1min} and its derived parameters showed the highest intra-TP correlations. ADC showed no correlation with other imaging parameters. For the inter-TP correlation, [^{18}F]FMISO was found to have the strongest self-correlation.

	ADC	iAUC	K^{trans}	A_{Brix}	DCE_{1min}	T2w	[^{18}F]FMISO
ADC	1						
iAUC	0.04±0.15	1					
K^{trans}	-0.06±0.18	**0.58±0.23**	1				
A_{Brix}	0.11±0.23	**0.42±0.25**	0.23±0.21	1			
DCE_{1min}	0.07±0.24	**0.57±0.21**	0.34±0.22	**0.48±0.34**	1		
T2w	0.12±0.13	0.03±0.15	0.02±0.12	0.03±0.12	-0.02±0.15	1	
[^{18}F]FMISO	-0.02±0.26	-0.04±0.19	0.03±0.15	-0.05±0.22	**-0.20±0.20**	0.03±0.15	1
Self-correlation with neighboring timepoints:							
TP to TP	0.23±0.28	0.19±0.23	0.15±0.23	N/A	0.29±0.24	0.22±0.21	**0.49±0.29**

Correlation coefficients close to 0 are depicted in gray. Correlations >0.4 are emphasized in bold. Negative correlations are shaded in gray.
TP to TP: mean of all assessed voxel by voxel self-correlation coefficients over all patients and timepoint pairs (BL-TP1, TP1-TP2, TP2-FU).
Abbreviations: ADC – apparent diffusion coefficient, iAUC – initial area under the enhancement curve, K_{trans} – transfer constant of the Tofts model, A_{Brix} – Amplitude of the Brix model, $DCE_{1\,min}$ – intensity of the dynamic contrast enhanced image 1 min after injection, T2w – intensity of the T2 weighted MRI, [^{18}F]FMISO - tumor to background ratio for [^{18}F]fluoromisonidazole signal.

Table 2 Score for local residual tumor based on MRI (radiologist), PET (nuclear physician), and PET-MRI (consensus radiologist and nuclear physician) performed 3 months after treatment, quantitative measurements, reference standard, and outcome

Patient	MRI_{post} ADC_{mean}	PET_{post} SUV_{max}	MRI residual	PET residual	PET-MRI residual	Reference standard: Local disease	Reference standard: Distant metastasis	Outcome
1	1.5	1.8	– –	–	– –	No	No	FU: NED 20 months
2	1.4	2.8	–	–	– –	No	No	FU: NED 26 months
3	1.3	2.9	–	+/–	– –	No	No	FU: NED 25 months
4	1.3	3.0	+	+	+/–	No	No	FU: NED 27 months
5	0.7	3.2	– –	+	–	Yes*	Yes	Palliation CHT
6	1.3	3.6	+	+ +	+ +	Yes	Yes	Palliation CHT, diseased
7	1.6	3.0	+	– –	+/–	No	Yes	Multiple meta, palliative
8	2.0	2.6	+/–	–	+	No	No	Salvage surgery, PA: no tumor. NED 21 months
9	1.5	5.1	+/–	+ +	+	Yes	No	Salvage surgery, FU: liver metastasis 3 months after surgery; palliative CHT
10	1.6	7.3	–	+	– –	No	Yes	Palliative CHT

Corresponding symbols: – –, definitely no residual tumor; –, probably no residual tumor; +/–, unclear possibly residual tumor; +, probably residual tumor; + +, definitely residual tumor/metastasis
Abbreviation: *PA* pathology, *NED* no evidence of disease, *FU* follow-up, *CHT* chemotherapy
*No pathology of local residual disease, growing mass on subsequent scans

- 3 months post RT
- FDG PET and T1/T2w/DWI

Table 3 Local residual tumor based on MRI (radiologist), PET (nuclear physician), and PET-MRI (consensus radiologist and nuclear physician) scores and change of opinion and policy

Patient	MRI local	PET local	MRI-PET local	Change of opinion (reason)	Policy of change
1	TN	TN	TN	–	–
2	TN	TN	TN	–	–
3	TN	Equivocal	TN	+ PET artifact	+ Follow-up
4	FP	FP	Equivocal	+ No PET uptake at suspicious MRI lesion	+ Additional imaging
5	FN	TP	FN	+ FDG uptake artifact at PET-MR	– Metastasis
6	TP	TP	TP	–	–
7	FP	TN	Equivocal	+ Consensus + MRI, non-suspicious PET	+ Additional imaging
8	Equivocal	TN	FP	+ Consensus PET-MR, PET hard to interpret due to low-FDG glucose uptake	+ Salvage surgery
9	Equivocal	TP	TP	+ MR partial volume, clear FDG uptake	+ Salvage surgery
10	TN	FP	TN	+ PET hotspot outside cervical tissue	– Metastasis

Abbreviation: *TN* true negative, *TP* true positive, *FP* false positive, *FN* false negative, + positive, – negative

Daniel M. et al. Impact of hybrid PET/MRI technology on multiparametric imaging and treatment response assessment of cervix cancer. Radio and Oncol 2017. 125:420-425
Mongula et al. PET-MRI for response assessment after radiation therapy of cervical carcinoma: a pilot study. EJNMMI Research 2018. 8:1
Khiewvan B. et al. Update of the role of PET/CT and PET/MRI in the management of patients with cervical cancer. Hellenic Journal of Nuclear Medicine 2016; 19(3): 254-268

Clinical Applications – Rectal Cancer

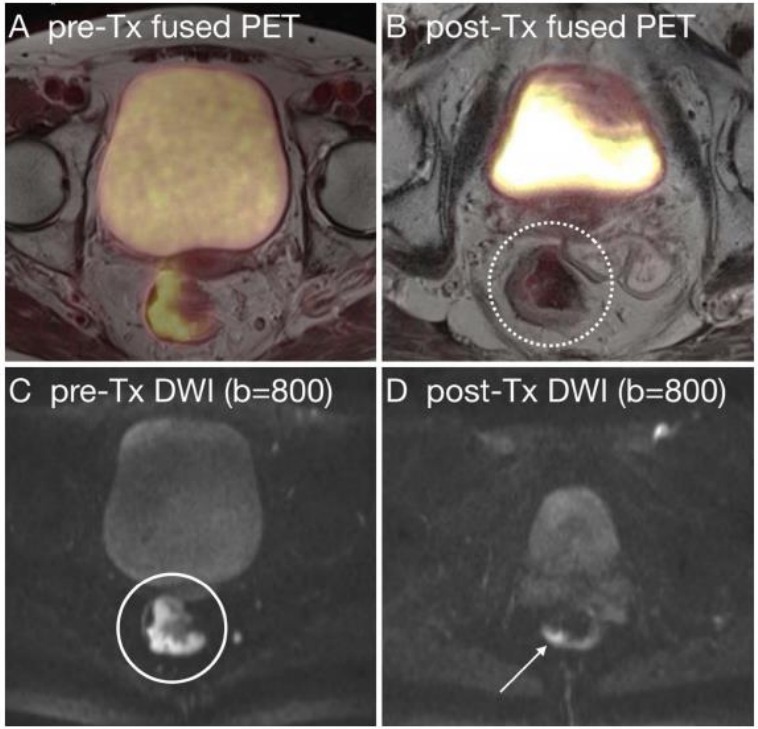

Fig. 6 A 72-year-old female with rectal adenocarcinoma before (**a**) and after chemoradiation (**b**). Post-therapy images suggest residual tumor on T2-weighted images, given that there was only a 24% reduction in tumor volume (**b**, white-dotted circle). FDG-PET shows a marked reduction in metabolic activity, with a reduction of the SUVmax from 13.7 to 4.5 (a 67% reduction). DWI images show a decrease in tumor that demonstrates restricted diffusion (**c**, white circle and **d**, white arrow). MRI indicated partial response on T2-weighted imaging, while PET imaging suggests potentially a complete response. At pathology this was confirmed a complete response

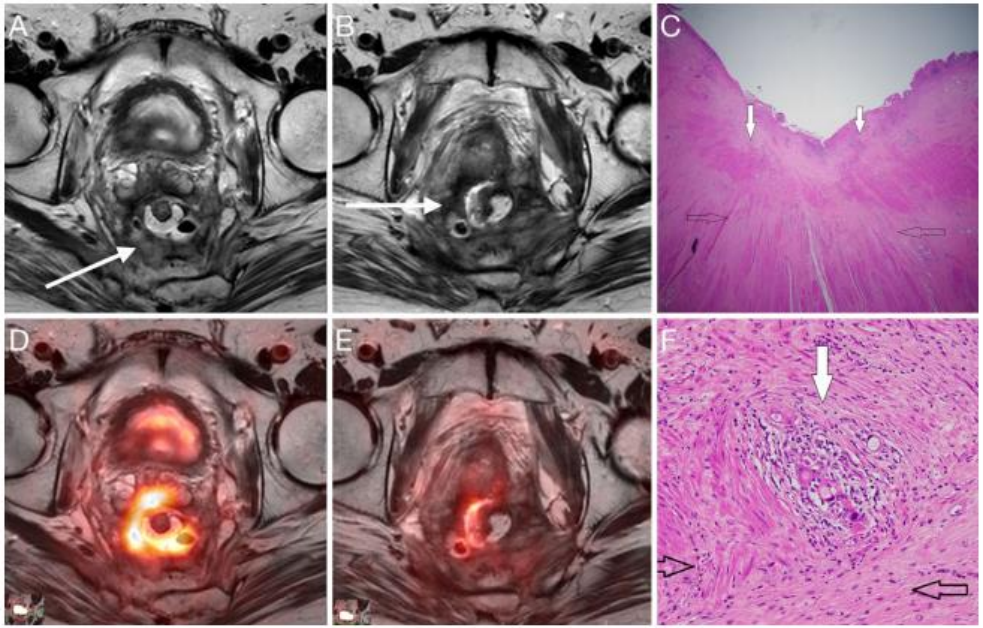

Fig. 7 PET/MRI performed in a 53-year-old man three years after surgery with a rising CEA. Axial T2 (**a**) demonstrates circumferential soft-tissue thickening with heterogeneously mixed hyperintense and hypointense signal intensity within the surgical bed (arrow). Fused axial PET image (**d**) demonstrates intense FDG uptake within this circumferential soft-tissue mass consistent with local recurrence. Inferiorly in the same patient, the MRI appearance is similar with semicircular T2 signal hypointensity (**b**, arrow), but FDG-PET demonstrates an absence of hypermetabolism (**e**) consistent with fibrosis. At pathology, one can see both recurrent tumor (**c** and **f**, white arrows) as well as fibrosis surrounding the region of local recurrence (**c** and **f**, open arrows). The addition of FDG-PET increases reader confidence and sensitivity for local recurrence

MAYO CLINIC

Hope TA, Kassam Z. et al. The use of PET/MRI for imaging rectal cancer. Abdominal Radiology 2019. 44:3559-3568

Clinical Applications – Head and Neck

- No generally accepted agreement on optimal time for imaging, but recommended:
  - 8-12 weeks after therapy
  - 12 months, 24 months (distant mets)
- PETCT versus PETMRI
  - No significant difference in detection of recurrence
  - PET/MRI may be superior to PET/CT in evaluating unclear FDG findings in follow-up patients
- PET/MRI Multi-parametric Studies
  - DWI has independent role from PET to determine tumor recurrence

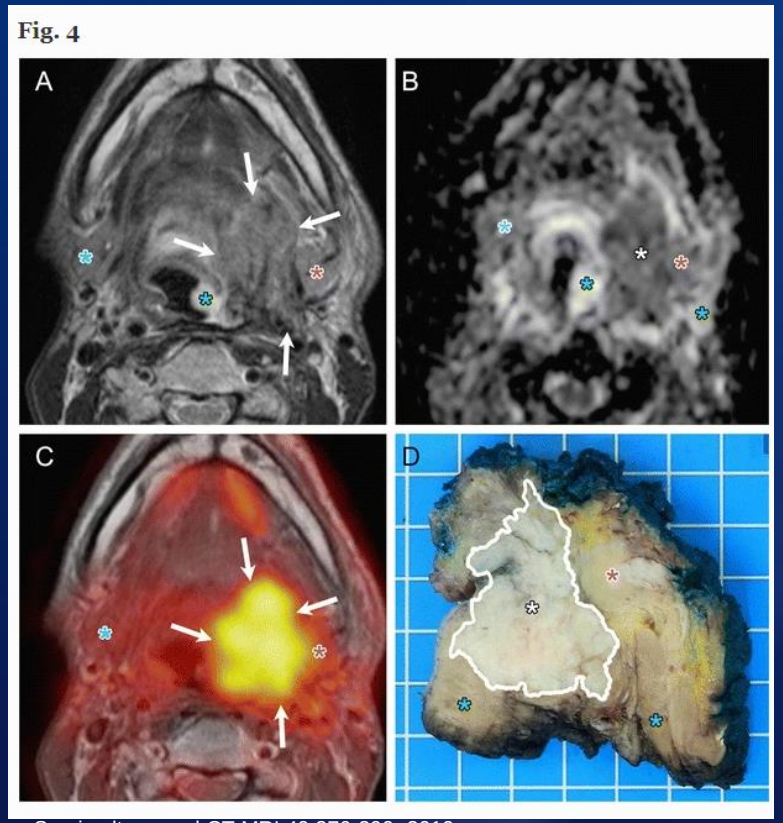

Ryan JL, Aaron VD, and Sims JB. PET/MRI vs PET/CT in Head and Neck Imaging: When, Why, and How. Semin ultrasound CT MRI 40:376-390. 2019
Queiroz, M. A., et al. PET/MRI and PET/CT in follow-up of head and neck cancer patients. *EJNMMI, 41*(6), 1066-1075. 2014
Queiroz, M. A., et al. Use of diffusion-weighted imaging (DWI) in PET/MRI for head and neck cancer evaluation. *EJNMMI, 41*(6), 2212-2221. 2014
Schaarschmidt et al. locoregional tumour evaluation of SCC in the head and neck: a comparison between MRI, PET/CT, and integrated PET/MRI. EJNMMI 43:92-102. 2016
Becker M et al. Local recurrence of SCC of the head and neck after radio(chemo)therapy: Diagnostic performance of FDG-PET/MRI with diffusion-weighted sequences. Euro Radiol 28:651-663.2018
Rasmussen JH et al. **Feasibility of Multiparametric Imaging with PET/MR in Head and Neck Squamous Cell Carcinoma**. JNM 1:69-74. 2017

PET-MRI – What's Next? PubMed Search

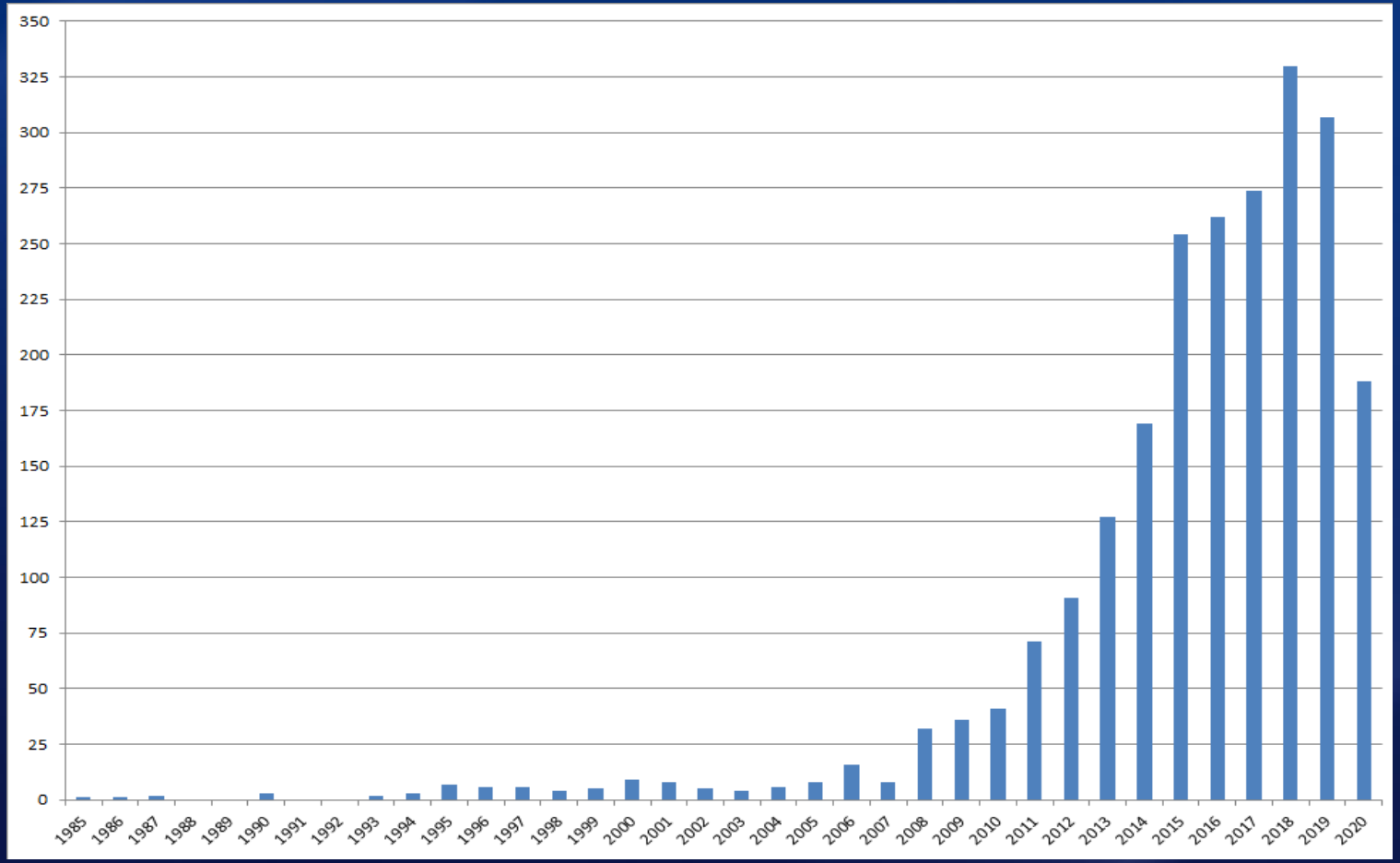

https://pubmed.ncbi.nlm.nih.gov/?term=PET-MRI&timeline=expanded

PET-MRI – What's Next? Clinical Trials

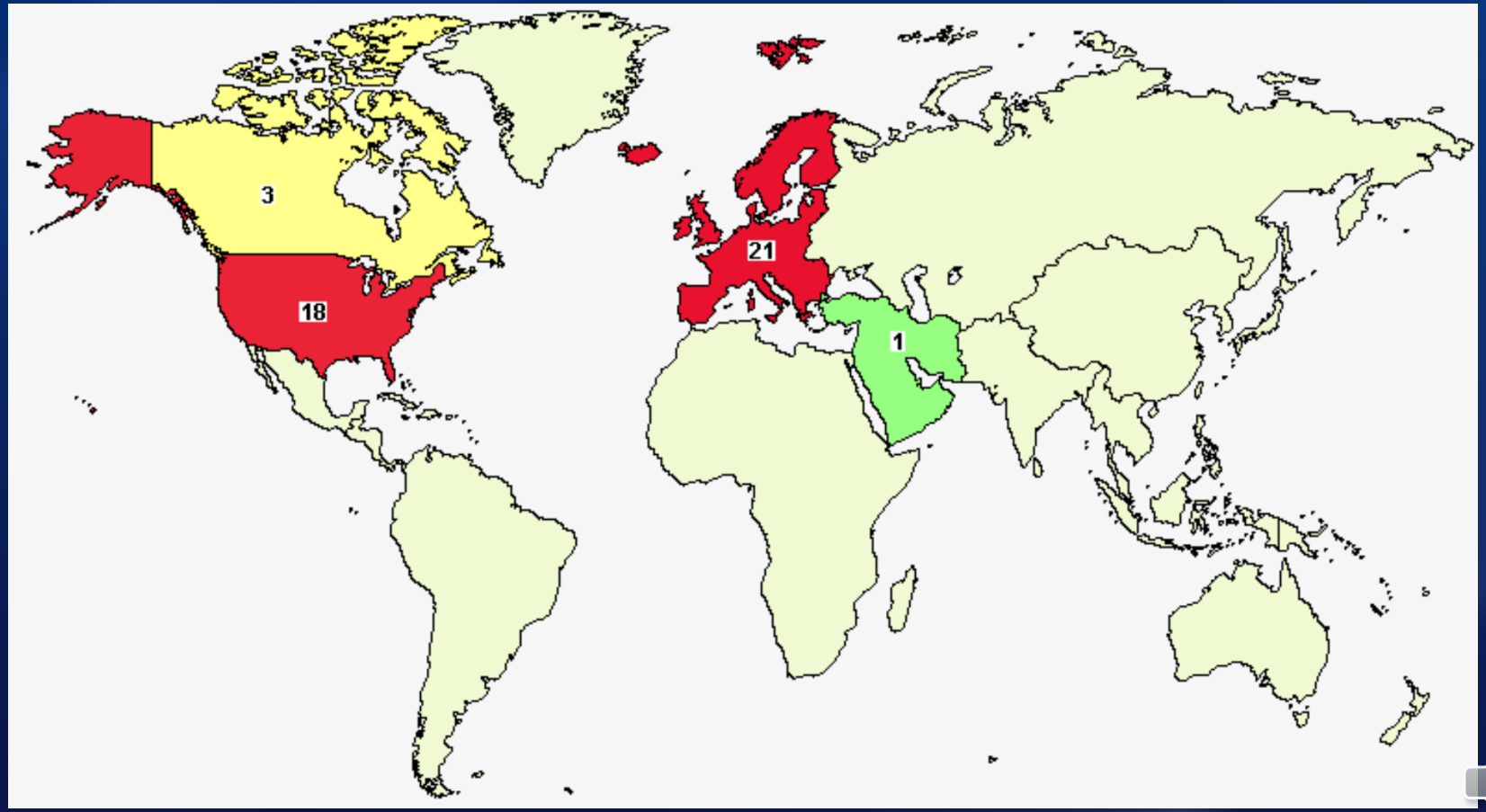

https://clinicaltrials.gov/ct2/results/map?cond=PET-MRI&map=

PET/MRI – What's Next?

- Continue to investigate improving techniques in technical challenges
- MRAC modeling
- Continued research looking at PET/CT (+/- MRI) versus PET/MRI, value added by each modality, cost, reimbursement, etc.
- Standardize clinical workflows and protocols
- Continued research to determine specific applications (e.g. diagnostic/staging, target delineation, treatment response assessment)/disease sites of PET/MRI technology for most benefit
- Qualifications for physicians, medical physicists, technologists

MAYO CLINIC

